Available online at www.sciencedirect.com
SCIENCE DIRECT®
PERGAMON
International Journal of Heat and Mass Transfer 46 (2003) 2637–2644
International Journal of HEAT and MASS TRANSFER
www.elsevier.com/locate/ijhmt

Influence of sleeve tube on the flow and heat transfer behavior at a T-junction

H.L. Wu [a,*], X.F. Peng [a], T.K. Chen [b]

[a] Department of Thermal Engineering, Tsinghua University, Beijing 100084, China
[b] School of Energy and Power Engineering, Xi'an Jiaotong University, Xi'an 710049, China

Received 15 May 2002; received in revised form 30 November 2002

Abstract

The flow structure of a sleeved jet into a main crossflow was experimentally investigated employing particle imaging velocimetry technology and numerically simulated using a CFD code. The jet-to-crossflow velocity ratio, VR, was ranged from 0.5 to 8. Three basic flow patterns were marked, namely attaching jet, lift-off jet and impinging jet as VR gradually increased. The flow in the main duct was characterized by a stream of discharge from the annular space at the rear part of the sleeve near the jet exit, which primarily came from the upstream crossflow. This annulus discharge isolated the leeward wall from the jet fluid and also caused weak local heat transfer in the large momentum deficiency region, and hence could supply an effective protection of the leeward wall from the thermal shock caused by a very cold jet injection.

Keywords: Jet-to-crossflow; Sleeve; Particle imaging velocimetry; CFD simulations; Thermal protection

1. Introduction

Jet-to-crossflow was extensively studied in the available open literature due to its importance in a wide variety of engineering fields [1–7], such as film cooling, discharge of waste water into river, fluid mixing in T-junction, and so on. However, few studies were reported on its variation forms, typically the sleeved jet into crossflow. In the primary cooling system of the pressurized water reactor (PWR), there exist a certain number of nozzles, e.g. the supply-line nozzle for the routine chemical and volume regulation and the safety-injection nozzle for emergency cooling. During plant operation, these nozzles are subjected to considerable thermal shocks caused by injection of water at a much lower temperature than that of the components and the coolant in the primary loop. To mitigate the thermally induced stress in nozzles, a protection tube, so-called thermal sleeve is sometimes integrated in a nozzle, or to say, a branch pipe [8–10]. The annulus between the sleeve and the nozzle, called sleeve annulus herein, isolates the nozzle from the cold jet fluid to reduce the thermal shock. It is of great interest for reactor designers to assess the structural and mechanical load on nozzles and to select adequate sleeve configuration for effective thermal protection. However, the choice of an appropriate design requires the knowledge of flow and heat transfer characteristics under various flow conditions. So far, such work is still of great shortage in the previous investigations [11,12]. Parras and Bosser [11] performed experiments to determine heat transfer parameters in such nozzles. Both the local heat transfer coefficients at the component inner wall and the fluid temperatures abutting on the wall were measured at several spots. However, due to the lack of the flow field data, their results are still not enough to further understand the flow mechanism.

In present work, experimental studies were carried out using a particle imaging velocimetry (PIV). The flow

* Corresponding author. Tel.: +86-10-6279-4942; fax: +86-10-6277-0209.
E-mail address: helen@te.tsinghua.edu.cn (H.L. Wu).

0017-9310/03/$ - see front matter © 2003 Elsevier Science Ltd. All rights reserved.
doi:10.1016/S0017-9310(03)00013-9

fields in the main duct and the sleeve annulus were visualized and measured, with the data serving to assess the fidelity and accuracy of the CFD simulations. The validated simulation results, combined with the experimental data, were then analyzed to understand the influence of the sleeve on the flow structure in the near wake and on the thermal shock upon the junction component.

2. Experimental rig

2.1. Test facility

The experiments were carried out in a close water loop with a main flow and a jet flow separately supplied, as shown in Fig. 1. The test section consisted of a main duct and a branch pipe including a sleeve tube inside and a cubical water basin outside. Both main duct and water basin were made of transparent acrylic Plexiglas, while the sleeve tube and the branch pipe made of transparent glass. The cutaway view of the cross section at the jet hole center from downstream and the A–A view are shown in Fig. 2. The main duct has a square inner cross section of 40×40 mm^2. The branch pipe has an inner diameter of 27.2 mm. The sleeve has an inner diameter of 13.2 mm and an outer diameter of 15.5 mm, resulting in a 5.9 mm wide annular gap between the sleeve and the branch pipe. Mesh screens were installed in the main duct at approximately 1.2 m upstream of the jet hole. The total flow was drained away from the main duct at about 0.6 m downstream. At the end of the main duct, a plane glass window was placed so as to allow optical access from downstream for measurements in the cross sections.

The test module included the supply-line nozzle integrated with a thermal sleeve as the prototype, which is commonly used in the PWR cooling system. The sleeve had two vent holes on both sides in the lower part, and had a collar near the jet exit with a narrow gap of 0.5 mm between the outer surface of the collar and the inner wall of the branch pipe. To reduce the optical distortion

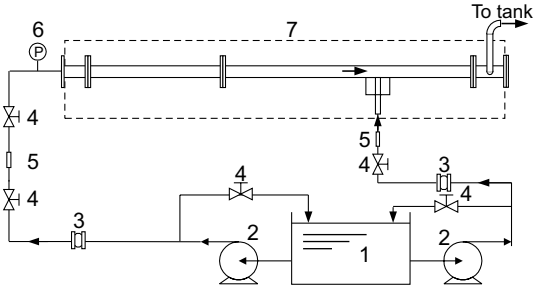

Fig. 1. Schematic diagram of test facility. (1) Water tank; (2) pump; (3) electromagnetic flowmeter; (4) valve; (5) filters; (6) manometer; (7) test section.

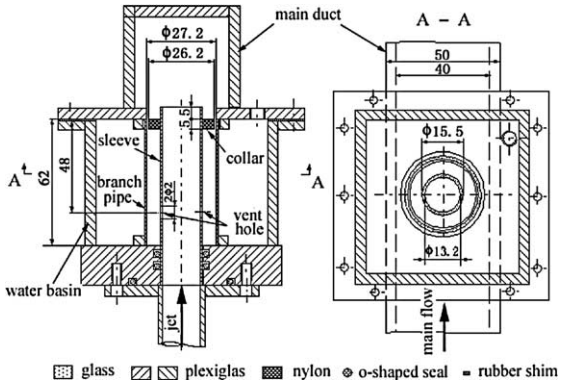

Fig. 2. Cutaway view of cross section at the jet hole center and A–A view (unit: mm).

Table 1
Flow parameters of testing runs

Run	VR	U_j (m/s)	Re_j	U_0 (m/s)	Re_0
1	0.5	1	16,431	2	99,580
2	2	2	32,861	1	49,790
3	4	4	65,723	1	49,790

due to the difference in refractive index of the transparent module and the fluid, the branch pipe together with the sleeve were embedded in a water basin with plane walls. The fluid in the water tank was preparatorily seeded with neutrally buoyant 5–10 μm CaC_2 ceramic powder. Table 1 lists the tested cases and corresponding parameters, where VR represents the jet-to-crossflow velocity ratio, Re_0 the crossflow Reynolds number, $Re_0 = \rho U_0 D_0/\mu$, and Re_j the jet flow Reynolds number, $Re_j = \rho U_j D_j/\mu$. Both the jet and crossflow were at same temperature of about 25 °C.

2.2. Particle imaging velocimetry

A commercial TSI incorporated PIV system was employed to measure the particle displacement within the laser sheet between two laser pulses. The flow field was illuminated by a thin laser sheet generated by a dual continuum surelite PIV-Lite 300 Nd:Yag laser. The particle images were recorded at each laser pulse by a 1018×1008 pixel CCD camera. Each pair of images were then divided into small square-shape interrogation sub-regions, where cross correlation was performed to determine the local velocity of the fluid, with the value assigned to the center. The time-averaged flow field was obtained by averaging 100 instantaneous vector maps processed from 200 images at one measurement sampling. To identify and remove outliers from a temporal series of processed PIV image velocity vectors, a procedure was developed utilizing both hard velocity cutoff limits and the Dixon criterion [13].

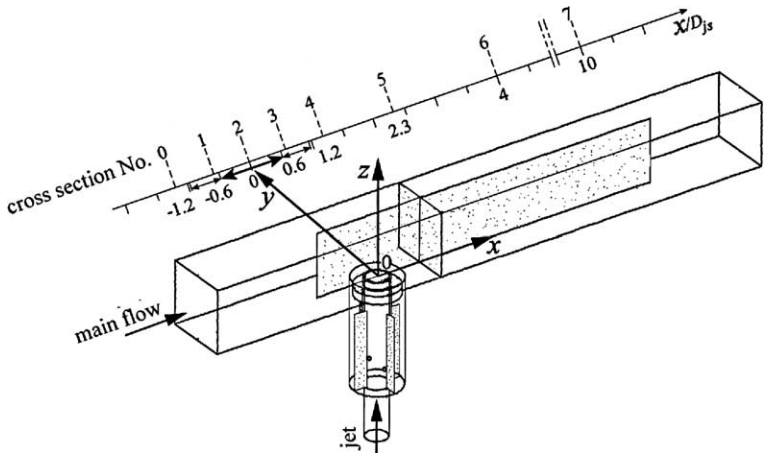

Fig. 3. Sketch map of the PIV measured positions.

Fig. 3 shows the sketch map of the PIV measuring locations. The right-handed Cartesian coordinate system was set up with its origin at the center of the jet hole and the positive X-axis in the streamwise direction. The streamwise, spanwise and vertical velocity components are denoted by U_X, U_Y, U_Z, respectively. The flow in the main duct was measured at the centric plane, and eight cross-sectional slices located at $X/D_j = -1.8$, -0.6, 0, 0.6, 1.2, 2.3, 4, 10, serially numbered 0–7. Among them, slice 2 located at the axis of the branch pipe, and slice 1 and 3 straddled the upstream and downstream annular space, respectively.

The effective viewing area was approximately 44×40 mm^2 (magnifying factor $M = 1$). The corresponding digital image size was about 950×870 pixels. Cross-correlation was performed with the sub-image size of 64×64 pixels with the neighboring sub-regions having 50% overlap, which resulted in the 40×40 grid of vectors with the in-plane resolution of 1 mm and the scale factor of 46 μm/pixel. With the particle displacement of 16 pixels, 1/4 of the sub-image size, the relative error in the displacement measurement was approximately $0.1/16 = 0.6\%$ [14]. For the centric plane about 160×40 mm^2 in size, the time-averaged velocity field was reconstructed by combining four slices in sequence with the conjoint strips interpolated.

3. CFD simulation

The CFD software FLUENT® was applied to obtain the flow behavior in the geometry corresponding to the PIV experimental model. One half of the domain was simulated because of symmetry. The Reynolds stress model (RSM) with wall-function approach was applied for turbulence modeling. The SIMPLEC pressure–velocity coupling algorithm was applied, and the second upwind scheme was used for the interpolation of the cell interfaces.

The computational domain extended in the streamwise direction from $7.58D_j$ upstream of the jet hole to $15.15D_j$ downstream, with the jet inlet located $7.58D_j$ below the jet hole. The whole computational domain was divided into four sub-domains for the convenience of grid establishing, marked sub-domain I–IV in Fig. 3. The conjunctional branch segment, sub-domain II, was of 3/5 height of the sleeve. Sub-domain II included the sleeve collar and sub-domain III the vent hole.

Unstructured hybrid meshes were applied. Most of the domain employed hexahedron grids except for sub-domain III. The process of grid generating in the whole domain is briefly described as follows. Firstly, the inlet plane of the main duct was meshed (Fig. 4a). Then the plane $Z = 0$ was delicately meshed, which included the bottom surface of the main duct, the end surface of the sleeve and the fluid pieces at that plane. The combination of the latter two was called the conjoint slice herein. The grid of the plane $Z = 0$ was then swept forward throughout the main duct to form the interior grid of sub-domain I (Fig. 4c). And then, the grid pattern of the conjoint slice was swept downward through sub-domain II. Partial grid of the sleeve grid is shown in Fig. 4d. And then, the grid of the jet inlet plane was carefully generated (Fig. 4b), and swept upward to mesh sub-domain IV. Lastly, sub-domain III was meshed with tetrahedron grids, with pyramid-shaped grids on its boundary surfaces, as shown in Fig. 4c. Fine grids were created in the near-wall regions and in the region near the jet discharge. The dimensions of the grids close to the walls varied slightly depending on VR to meet the wall-function approach demands. Grid dependency tests showed that although fully grid-independent results were difficult to obtain, the present computations were not substantially different from those calculated on a grid about twice as fine in the domain.

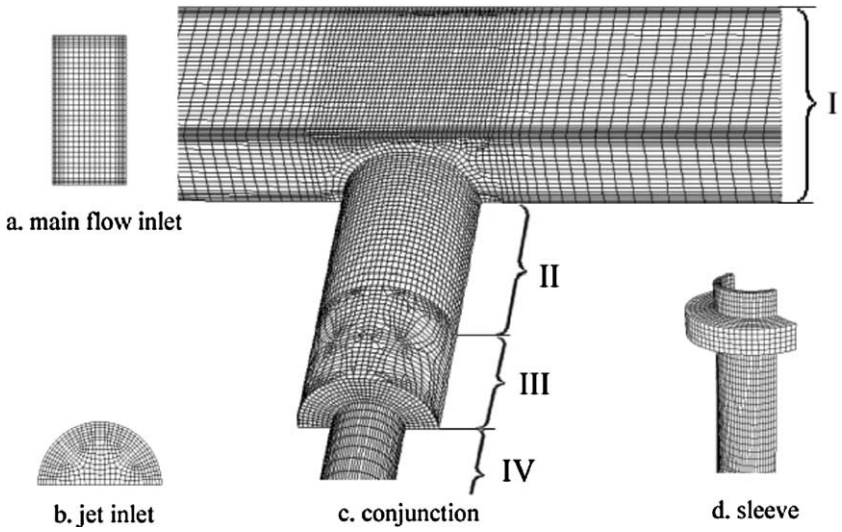

Fig. 4. Unstructured grids schematic.

Four types of boundary conditions were encountered: inlet, outlet, symmetry and wall. The inlet mean velocity of the crossflow and jet, U_0 and U_j, were referred to the PIV experiments (Table 1). The profiles of the velocity and turbulence parameters of the oncoming crossflow were prescribed from preliminary simulation of the flow in an upstream main duct about $30D_0$ long. Similar treatment was also performed for the oncoming jet flow assignment. Small temperature difference was artificially introduced, with the temperatures of both crossflow and jet being 320 and 300 K, respectively. All the duct walls were set to be adiabatic whereas the sleeve was thermally coupled with the fluid.

4. Results and discussion

4.1. Validation

Once the experimental data were obtained, the measured flow fields were qualitatively compared with the simulation results. Fig. 5 shows the comparison of the streamwise velocity profiles in the centric plane at six locations with VR = 2. At all locations where X/D_{js} is no greater than 0.8, quite good agreement is reached between the two sets of results, except for small difference in the momentum deficient zone. Compared with the experimental data, the computations show a stronger reverse flow at $X/D_{js} = 0.8$, and a slower recovery of momentum thereafter. Moreover, the experiments display a bigger nose corresponding to the maximum streamwise velocity, indicating less turbulent dissipation of the jet momentum or larger entrainment of the surrounding fluid. However, the consistency between the two results is well recognized and the computations could be considered credible.

A picture is presented in Fig. 6a to illustrate the flow regime, where the flow was visualized with a small amount of air introduced through a very narrow seam at the intersecting line between the branch pipe and the main duct. The corresponding computed trajectory lines are shown in Fig. 6b, which originate from the jet hole and a ring just above the sleeve collar. The essential flow features are qualitatively in good agreement.

4.2. Flow structures and heat transfer behavior

Previous investigations of the jet-to-crossflow without sleeve showed that the most crucial factor affecting the flow pattern was VR [15,16]. This also holds for the sleeved jet-to-crossflow situation. Three basic flow patterns could be marked in the main duct, namely attaching jet, lift-off jet and impinging jet, as VR gradually increases. Fig. 7 displays the simulated and measured streamline patterns in the centric plane, reconstructed from the in-plane flow field by path integration. The distributions of the spanwise vorticity, $\Omega_Y = \partial U/\partial Z - \partial U_Z/\partial X$, are also shown by gray-level contours. The upstream and leeward collar annuli are denoted to the sunken space over the sleeve collar in the centric plane. The resemblance of these two sets of results is evident for all VR cases.

For a small VR of 0.5, the jet was strongly oppressed by the oncoming crossflow. The flow of jet over the jet hole was greatly deformed, with the jet mostly discharging from the lee part of the hole. The jet was oppressed into the region near the bottom wall, forming the so-called attaching jet. For VR increased to an intermediate value of 2, the jet lifted off the bottom wall to

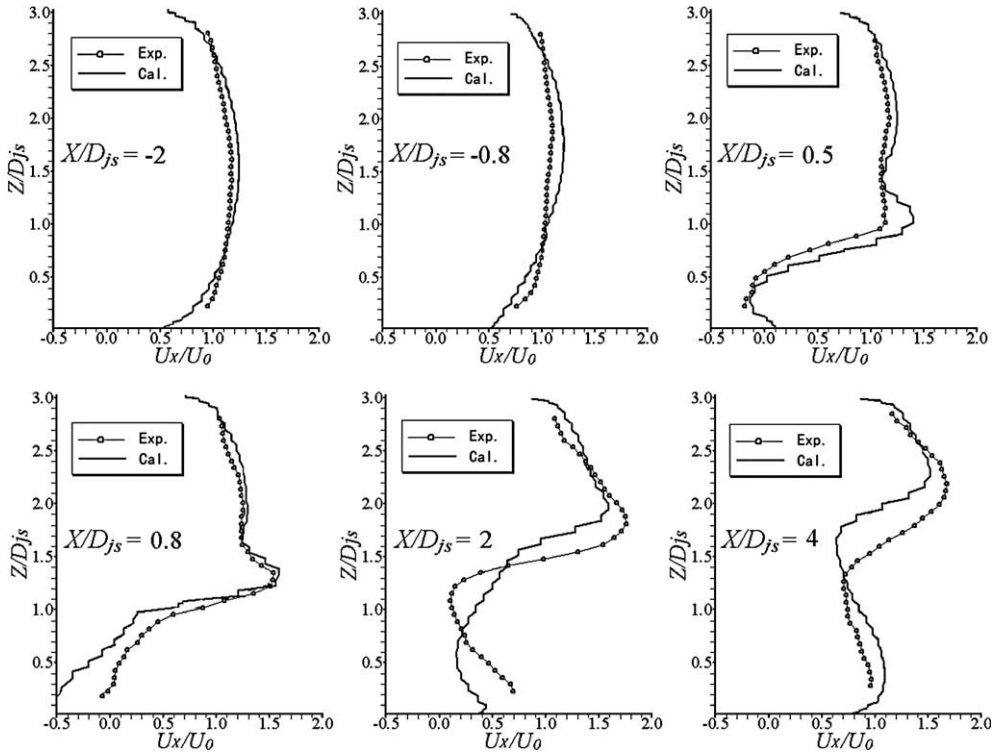

Fig. 5. Comparison of measured with computed streamwise velocity profiles (VR = 2).

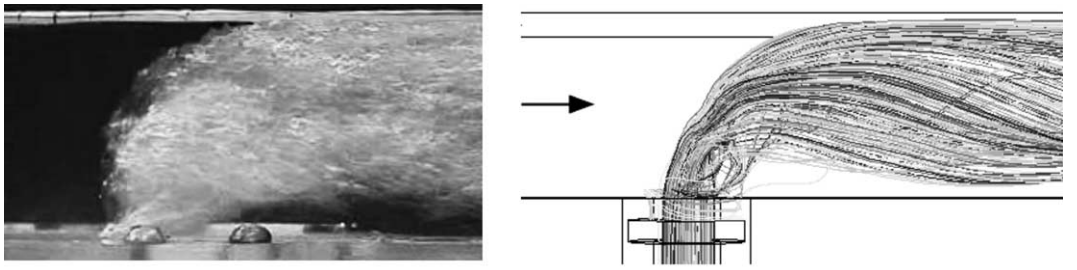

Fig. 6. Comparison of flow visualization with computed trajectory lines (VR = 4). (a) Photo of flow visualization; (b) numerically simulated trajectory lines.

develop into the crossflow. When VR = 4, the jet further penetrated through the crossflow approaching to the opposite wall. The discharge velocity over the jet hole came to be rather uniform. At an even high VR of 8, the jet impinged on the opposite wall and formed a large recirculating flow region upstream of the impingement point near the top wall (Fig. 7c). The backwash of the impinging jet caused the crossflow boundary layer separate from the top wall and detour below. Downstream, stratified flow regime was formed with the jet fluid rapidly developing near the top wall.

At the leading and trailing boundaries of the issuing jet, intensive vorticity could be found with opposite signs, which originated from the circumferential shear layer vorticity inside the sleeve tube. The vorticity shedding and rolling-up could be observed from the temporal series of instantaneous vector maps acquired from 100 image pairs. The upstream sunken collar annulus showed little influence on the jet flow behavior. However, the leeward collar annulus played an important role. Specifically, there was a stream of discharge from the annular space at the rear part of the sleeve near the jet exit, referred as the *annulus discharge*, forming a secondary discharge into the crossflow except for the jet itself. This led to greater momentum deficiency at the lee side, and further weakened the local heat transfer.

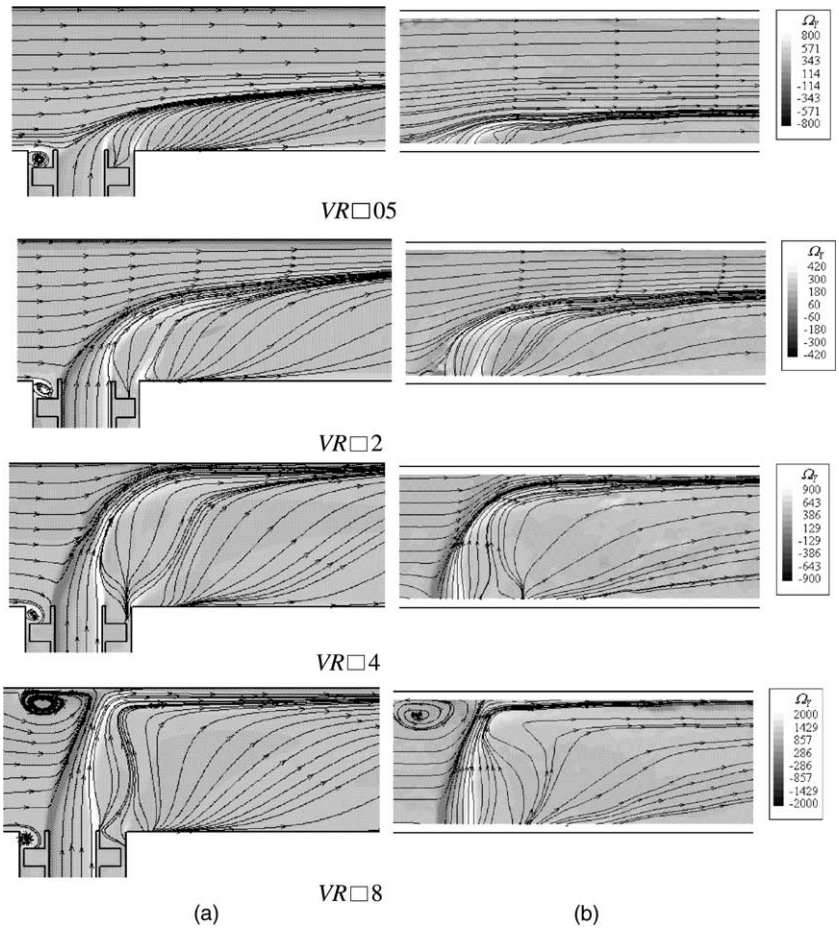

Fig. 7. Comparison of streamline pattern and streamwise vorticity in the centric plane. (a) Simulated results; (b) experimental data.

Fig. 8 presents vector maps, contours of streamwise vorticity Ω_X and normalized temperature θ at six cross sections when VR = 2, where $\Omega_X = \partial U_Z/\partial Y - \partial U_Y/\partial Z$, $\theta = (T_0 - T)/(T_0 - T_j)$. At the cross section $X/D_{js} = -0.5$, part of the upstream crossflow went downward into the upstream collar annulus. At the cross section $X/D_{js} = 0$, strong streamwise vorticity shedded from the sides of the jet, and developed upward and laterally. As the jet bended gradually, the spanwise leading vorticity of the jet realigned to the streamwise direction, resulting in the increase of the streamwise vorticity at the cross section $X/D_{js} = 0.5$. Remarkable vorticity appeared below these shear layer vorticity, but having an opposite direction. The interaction between the two pairs of vorticity led to the movement of the annulus discharge fluid from the bottom up to the central plane, as demonstrated in Fig. 8d, where the θ contours was hollowed from the inner bend of the *kidney* shape. Since most of the annulus discharge came from the crossflow, this intrusion greatly diluted the jet fluid in the vicinity of the symmetry plane. Its further transportation by the upper counter-rotating vortex pair accelerated the formation of the deep concave of the θ contours, and effectively attenuated the influence of the jet upon the leeward wall. The concentrated vorticity dissipated rapidly downstream of cross section $X/D_{js} = 2$.

Fig. 9 displays the perspective trajectory lines originating from the fluid cell adjacent to the outer surface of the sleeve and the inner surface of the branch pipe. The fluid in the upstream sleeve annulus progressed spirally in the sleeve collar annulus. It finally turned upward into the main flow and formed a wrapping skirt at the leeward boundary of the issuing jet. This illustrated the primary mechanism of the annulus discharge formation. Moreover, a kink-shaped bundle of trajectory lines could be observed in the leeward collar annulus in the top view, showing the rewind of part of the annulus discharge stream, while the side view indicates the upward entrainment of this stream by the jet. Therefore, the annulus discharge was actually a kind of very complicated three-dimensional spiral-shaped recirculating flow. If the jet injects into the crossflow at a temperature

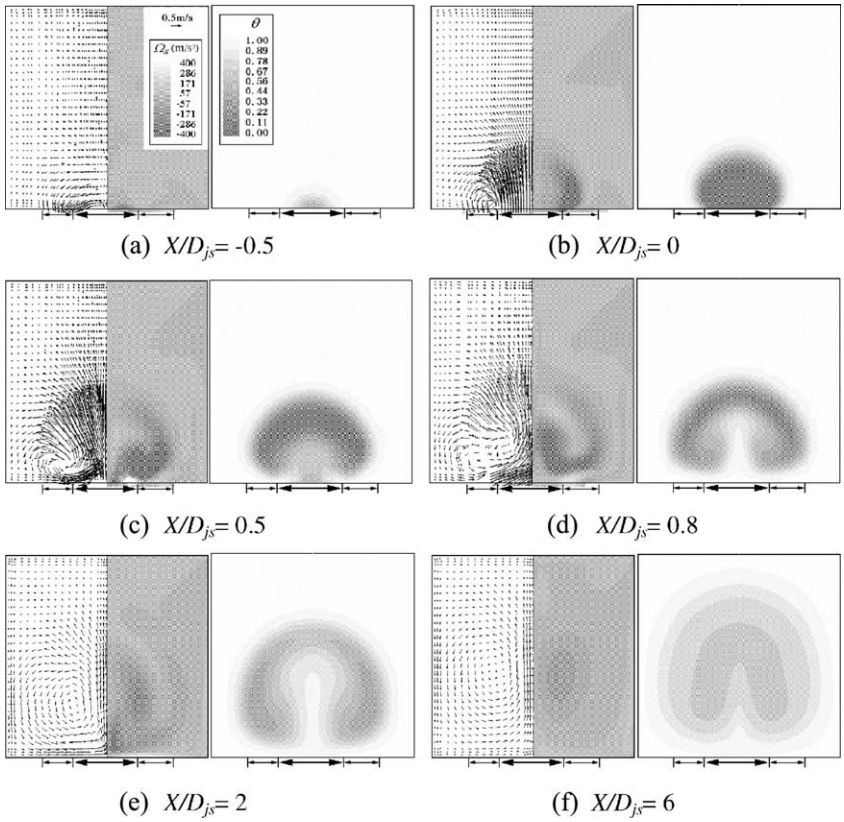

Fig. 8. Vector maps, contours of Ω_X and θ at six cross sections (VR = 2). (a) $X/D_{\mathrm{js}} = -0.5$; (b) $X/D_{\mathrm{js}} = 0$; (c) $X/D_{\mathrm{js}} = 0.5$; (d) $X/D_{\mathrm{js}} = 0.8$; (e) $X/D_{\mathrm{js}} = 2$; (f) $X/D_{\mathrm{js}} = 6$.

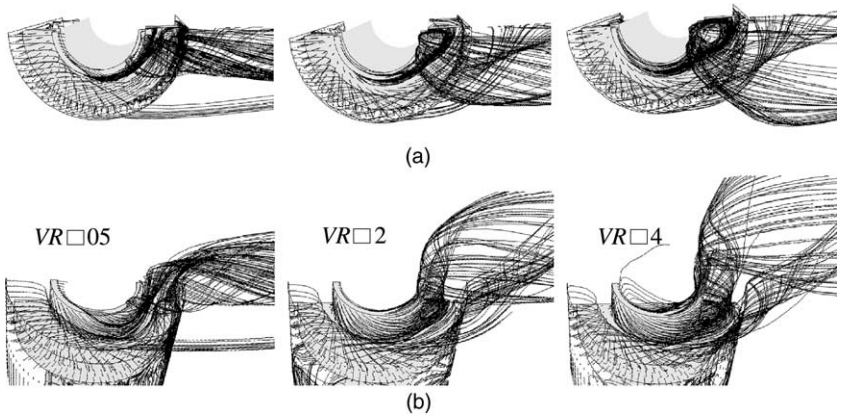

Fig. 9. Trajectory lines near the sleeve annulus. (a) Top view; (b) side view.

much lower than the crossflow, the annulus discharge would supply an effective thermal protection of the leeward wall from the thermal shock at two aspects: isolation of the leeward wall from the jet fluid and attenuation of local heat transfer in the leeward momentum deficiency region.

5. Conclusions

The flow structure of a sleeved jet into crossflow was experimentally investigated employing PIV and numerically simulated using CFD code with the jet-to-crossflow velocity ratio, VR, being 0.5–8.

(a) The most crucial factor affecting the flow pattern was VR. Three basic flow patterns were marked, namely attaching jet, lift-off jet and impinging jet as VR gradually increased. The computations well matched the experimental results.
(b) A stream of discharge from the downstream sleeve annular space, indicated as the *annulus discharge*, formed a secondary discharge into the crossflow except for the jet itself. It was a kind of complicated three-dimensional spiral-shaped recirculating flow. In the case of a very cold jet injection, the annulus discharge would supply an effective thermal protection of the leeward wall from the thermal shock at two aspects: isolation of the leeward wall from the jet fluid and attenuation of local heat transfer in the leeward momentum deficiency region.

References

[1] R.J. Goldstein, J.R. Taylor, Mass transfer in the neighborhood of jets entering a crossflow, J. Heat Transfer 104 (4) (1982) 715–721.
[2] S. Wittig, V. Scherer, Heat transfer measurements downstream of a two-dimensional jet entering a crossflow, J. Turbomachinery 109 (4) (1987) 572–578.
[3] K.A. Thole, M. Gritsch, A. Schulz, S. Wittig, Effect of a crossflow at the entrance to a film-cooling hole, J. Fluids Eng. 119 (3) (1997) 533–540.
[4] M.J. Findlay, M. Salcudean, I.S. Gartshore, Jets in a crossflow: effects of geometry and blowing ratio, J. Fluids Eng. 121 (2) (1999) 373–378.
[5] T.F. Fric, A. Roshko, Vortical structure in the wake of a transverse jet, J. Fluid Mech. 279 (1) (1994) 1–47.
[6] C. Brucker, Study of the three-dimensional flow in a T-junction using a dual-scanning method for three-dimensional scanning-particle-imagine velocimetry (3-D SPIV), Exp. Thermal Fluid Sci. 14 (1) (1997) 35–44.
[7] J.H. Kim, An analytical mixing model for buoyant jet injected into pipe flow, J. Heat Transfer 107 (3) (1985) 630–636.
[8] B.L.J. Dow, A.R. McIlree, SG repair has something up its sleeve, Nucl. Eng. Int. 43 (524) (1998) 36–38.
[9] K.R. Rousseau, S. Palmer, R.C. Harvey, P.A. Bergeron, Maine Yankee steam generator tube sleeving thermal-hydraulic and safety analysis impacts, in: Proceedings of the American Power Conference, Part 2, Illinois Inst of Technology, Chicago, 1996, pp. 779–782.
[10] S.W. Glass, D.M. Schlader, Inspection and repair techniques and strategies for alloy 600 PWSCC in reactor vessel head CRD nozzles and welds, in: ICONE-vol. 1, ASME, New York, 2002, pp. 421–427.
[11] F. Parras, M. Bosser, Heat transfer in pressurized water reactor components most often subject to thermal shock, Nucl. Technol. 47 (1) (1980) 125–152.
[12] K. Kussmaul, W. Mayinger, Numerical and experimental analyses of the behaviour of a nozzle with thermal sleeve under stratified flow, Nucl. Eng. Design 190 (1) (1999) 127–140.
[13] W.J. Dixon, F.J. Massey, Introduction to statistical analysis, fourth ed., McGraw-Hill, New York, 1983.
[14] M.P. Wernet, Application of DPIV to study both steady state and transient turbomachinery flows, Optics Laser Technol. 32 (7–8) (2000) 497–525.
[15] J. Andreopoulos, W. Rodi, Experimental investigation of jets in a crossflow, J. Fluid Mech. 138 (1) (1984) 93–127.
[16] L.L. Yuan, R.L. Street, J.H. Ferziger, Large-eddy simulations of a round jet in crossflow, J. Fluid Mech. 379 (1) (1999) 71–104.